Graphene Ribbon Growth on Structured Silicon Carbide

Alexander Stöhr[1], Jens Baringhaus[2], Johannes Aprojanz[2], Stefan Link[1], Christoph Tegenkamp[2], Yuran Niu[3,4], Alexei A. Zakharov[3], Chaoyu Chen[5], José Avila[5], Maria C. Asensio[5], and Ulrich Starke[1]*

Structured Silicon Carbide was proposed to be an ideal template for the production of arrays of edge specific graphene nanoribbons (GNRs), which could be used as a base material for graphene transistors. We prepared periodic arrays of nanoscaled stripe-mesas on SiC surfaces using electron beam lithography and reactive ion etching. Subsequent epitaxial graphene growth by annealing is differentiated between the basal-plane mesas and the faceting stripe walls as monitored by means of atomic force microscopy (AFM). Microscopic low energy electron diffraction (μ-LEED) revealed that the graphene ribbons on the facetted mesa side walls grow in epitaxial relation to the basal-plane graphene with an armchair orientation at the facet edges. The π-band system of the ribbons exhibits linear bands with a Dirac like shape corresponding to monolayer graphene as identified by angle-resolved photoemission spectroscopy (ARPES).

1 Introduction

Graphene is considered to be a possible successor of silicon for applications in the semiconductor industry. However, an extended graphene layer does not exhibit a bandgap, which would be crucial for the usage of graphene in logical circuits. To date, a number of techniques are considered for inducing a band gap in graphene – among those a distinction of the A- and B-lattices, e.g. by doping and/or inducing spin-orbit interaction. Nevertheless, one of the most promising techniques is the confinement of graphene's charge carriers into one-dimensional stripes, so called graphene nanoribbons (GNRs). In 1996 Nakada et al. studied theoretically the influence of the edges on the transport properties through GNRs [1]. According to this early investigation, only GNRs with a so-called armchair like, perfectly ordered atomic configuration at the edges are predicted to be

semiconducting. However, structuring the graphene using conventional lithography techniques cannot realize this situation, since it leads to defects and disorder at the edges. Although experimentally a band gap was observed in narrow ribbons [2], it turned out that this gap appears to be due to the presence of disorder-induced quantum dots [3]. Another technique to create GNRs is the chemical vapor deposition of molecules on a metallic substrate and subsequent synthesis to ribbons, which produces specific edges [4, 5]. However, this technique has the disadvantage of the presence of a metallic substrate, which would lead to parasitic currents through the conducting layer beneath the graphene which in turn could only be overcome by a subsequent ribbon transfer after growth. To circumvent both problems, we use a new approach which is to grow graphene ribbons on structured SiC [6–8]. Since SiC itself has a large bandgap so that the graphene is grown on a quasi-insulator, no parasitic currents are expected to flow across the substrate. Beside this, since the structuring process on the substrate happens before the graphene growth, no mechanical disruption of the graphene edges occurs [6]. Trenches of a few nanometer in depth are processed into the SiC surface so that a periodic array of mesas, trenches and side walls is generated. The period of this structure can be decreased down to the 20-50 nm regime. By annealing the structured SiC sample different graphene species can be grown on the different components of the struc-
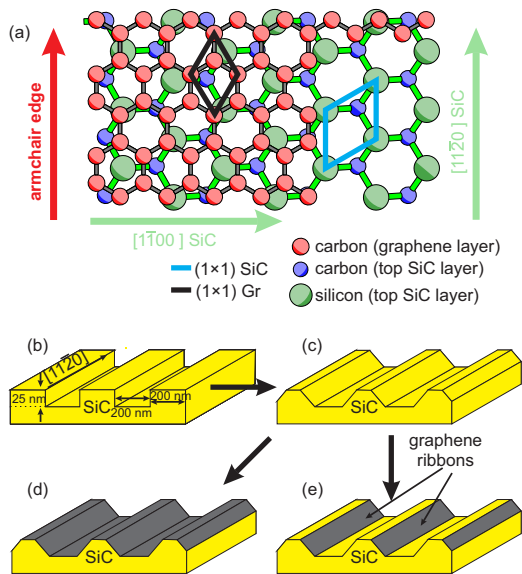
Figure 1 (a) Ball and stick model of the graphene buffer layer on the SiC(0001) surface (top view). The graphene and SiC unit cells are highlighted by black and blue hexagons, respectively. Due to the strong interaction of the first carbon layer with the SiC(0001) surface, graphene grows epitaxially with a fixed 30° angular orientation with respect to the substrate. (b-e) Schematic illustration of the annealing process of the structured SiC crystal: (b) Lithographically structured SiC crystal with trenches running along the [11$\bar{2}$0]-direction of the SiC. (c) After annealing the sample at 900 °C for 30 min the sidewalls relax into facets. (d) Structured sample after full graphitization. (e) The desired preferential graphene growth on the sidewalls, which would lead to isolated graphene nanoribbons on the facets.

tured array. On the SiC(0001) surface epitaxial graphene grows with a fixed orientation with respect to the substrate [9, 10] and therefore by choosing the right orientation of the trenches, either armchair or zigzag terminated GNRs can be produced as illustrated in Fig. 1 (a). This model assumes that the growing GNRs continue the graphene orientation from the lower or upper terraces. In the present work we focus on the graphene growth of armchair GNRs.

2 Experimental

We use 6H-SiC(0001) wafers as a substrate purchased from the company SiCrystal. These crystals are initially flattened by means of hydrogen etching in a quartz-glass

furnace at a temperature of about 1500 °C and a hydrogen pressure of 1 bar [11]. Afterwards, the surface is covered with the electron beam resist ZEP (ZEON chemicals). The resist is illuminated in stripes along the [11$\bar{2}$0]-direction of the SiC surface. Here, we used a stripe periodicity of 400 nm. Subsequently, the illuminated and developed resist is removed and the pattern of the remaining resist is transferred 25 nm deep into the SiC by means of reactive ion etching. Finally, the patterned SiC crystal is cleaned from the residual resist by rinsing in acetone, cf. Fig. 1 (b). After the patterning, graphene is grown on the structured sample.

The growth temperature for the graphene ribbons on these samples turned out to be critical. In the traditional procedure of annealing in ultra-high vacuum (UHV) [12] the growth temperature is too low which leads to inhomogeneous graphene growth. On the other hand, the advanced method of annealing in Ar atmosphere which yields extremely homogeneous graphene on unstructured basal plane surfaces [10, 13] requires temperatures in the 1500 °C regime, which is too high so that the SiC becomes quite volatile, and the trenches are flattened out (see AFM images in Fig. S1 of the supporting information). In order to realize annealing temperatures, which lie in between those extremes, the samples are annealed under UHV-conditions in a face to face geometry [14]. In this technique, two samples facing each other are brought into close proximity (250μm) to each other. During the annealing step using this so-called face-to-face method, the samples provide each other with a silicon background pressure, which slows down the silicon sublimation rate and allows the growth of a homogenous graphene layer without flattening the samples. Thereby, the annealing growth process on this structured surface is divided into two sub-steps [15]. In the first step, the SiC samples were annealed at 1200 °C for 30 min to enable a sufficient SiC mass transport, which leads to a relaxation of the sidewalls into facets as sketched in Fig. 1 (c). In the second step, the annealing temperature is increased to around 1400 °C for 10 minutes to start selective graphene growth, cf. Fig. 1 (d)&(e). By varying details of the annealing parameters (time, temperature) one can influence whether graphene grows only on the facets, as indicated in Fig. 1 (e), or if the graphene layer covers the mesa structure as well, as sketched in Fig. 1 (d). Note that the required temperature may depend on the face-to-face setup, and in addition the temperature is measured on the backside of the sample, so that the exact reading may vary.

The morphology of the samples was investigated by means of atomic force microscopy (AFM) in ambient conditions. Local ordering was analyzed by low-

energy electron microscopy (LEEM) and microscopic low-energy electron diffraction (μ-LEED) at the I311 beamline of the Max-lab synchrotron facility in Lund, Sweden. The electronic structure was determined using angle-resolved photoemission spectroscopy (ARPES) at the ANTARES beamline of the SOLEIL synchrotron in Gif sur Yvette, France and at beamline UE112-PGM-1[2] at the BESSY-Synchrotron of the Helmholtz-Zentrum Berlin (HZB), Germany.

3 Results

Immediately after the growth process the samples were investigated with AFM. In Fig. 2 (a) the AFM-topography is displayed. The stripe pattern with perfectly straight lines separating the different components of the mesa structure is still visible after the annealing procedure. Notably, a relaxation of the sidewalls into tilted, ribbon-like planes (facets) can be seen in the AFM-topography and especially well in the line profile shown in Fig. 2 (c). From these line profiles, the faceting angle can be extracted and this angle (of the order of 26°) is similar to the angles which were reported from other groups for faceted sidewalls oriented along the [1$\bar{1}$00]-direction of the SiC [6, 7, 15, 16]. With an etching depth of 25 nm the inclination angle translates into about 60 nm wide sidewall stripes which we indeed covered with graphene as discussed below. These graphene ribbons are still too wide to produce a sizable band-gap. However, for the investigation of the graphene properties using modern surface science techniques, they are well-suited. Using a different AFM acquisition mode we investigated the local change of the contact potential difference (CPD). On a flat epitaxial graphene sample on SiC(0001), one can easily distinguish between zerolayer (ZLG), monolayer (MLG) and bilayer graphene (BLG) via the contact potential difference (CPD) [17]. For such graphene slabs it was reported, that the CPD increased by about 135 meV for each additional graphene layer on a flat SiC sample. Fig. 2 (b) displays a CPD map, which was acquired on the same area as in Fig. 2 (a). Also in this CPD map, areas with different CPS-signal strength can be determined. Notably, in the trenches a higher CPD signal is detected, which presumably is connected to the rougher trench bottom after the plasma etching process, i.e. in these areas the SiC decomposition may proceed faster resulting in an increased graphene signal. However, comparison of the topography and CPD line profiles as shown in Fig. 2 (c) – focused in detail on the transitions between mesa and trench, reveals an enhanced CPD-signal on the sidewalls.
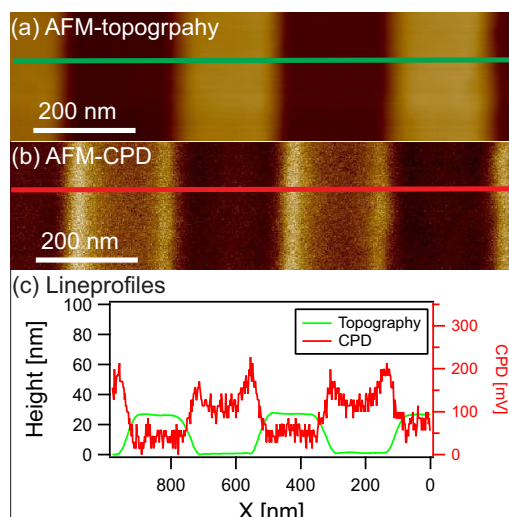

Figure 2 AFM topography and map of the local variation of the contact potential difference (CPD) of the structured and graphitized sample. (a) In topography the bottom of the trenches appear in darker colors. The facets are observable due to the smooth color transition between the trenches and mesas. (b) CPD signal of the structured SiC sample after graphitization, suggesting an enhanced graphene growth on the facets. Also in the trenches the graphene growth rate appears larger than on the mesas. (c) Line profiles of the topography and the CPD taken at the indicated areas. A facet angle of the sidewalls of about 26° can be extracted from the topography line profile. The strongest CPD signal can be pinned to the faceted regions.

On these areas the CPD-signal is about 130 meV larger than the CPD-signal on the flat areas suggesting a thicker graphene layer on the sidewall facets. It should be noted, however, that such an effect may also originate from a geometrical feature and therefore it is only a hint for a potentially enhanced graphene growth on the sidewalls.

The local order of the structured and graphitized sample was investigated by means of μ-LEED – also in order to exclude the possibility that the enhanced CPD signal is due to excessive amorphous carbon agglomerated on the facets. Fig. 3 (a) displays a μ-LEED pattern obtained on a structured surface using a beam of about 1.3 μm in diameter after introduction into UHV and outgassing at about 600 °C. The first order graphene and SiC diffraction spots are indicated with black and red arrows, respectively. Also, the $(6\sqrt{3} \times 6\sqrt{3})$R30° superstructure spots are visible, which are typical for graphene grown on the SiC(0001) basal plane. Besides the ordered

basal plane pattern, faceting streaks can be noted (orange arrows) which are a first proof for the faceting on the basal plane sample. In addition, some diffraction spots (marked with orange circles) appear in proximity to the SiC and superstructure spots. From the orientation of the faceting streaks and spots with respect to the normal graphene and SiC spots one can confirm the orientation of the facets to be along the armchair direction. In a conventional LEED experiment the motion direction for the facet streaks and spots across the LEED screen is different from the motion of the regular spots, when the energy is changed. In the μ-LEED instrument the normal surface spots maintain their position on the detector, since the momentum scale remains constant, only the facet features change their position when varying the energy. In this way the reciprocal diffraction rods can be directly imaged in an energy series. For diffraction spots coming from inclined surface areas, like facets, the diffraction rods are inclined with respect to the rod of the non-faceted areas [18]. In Fig. 3 (b) line profiles taken at the area indicated by the green rectangle in (a) are plotted for electron beam energies from 30 to 45 eV. The two vertical diffraction rods arise from a first order SiC spot and a reconstruction-superstructure spot from the non-inclined surface area, respectively. A series of weaker rods, which are inclined in comparison to the vertical rods, originate from the facets. They document crystalline order of the graphene grown on those facets. They show in addition, that the graphene on the facets has the same angular orientation with respect to the substrate as graphene grown on a flat SiC(0001) sample.

From a structural point of view, the graphene ribbon on the sidewall facet grows in the desired geometry, flat on the facet and in the proper orientation for armchair edges. For the respective examination of the electronic properties of the graphene layer on the facets, the band structure was measured using ARPES at the ANTARES beamline at the SOLEIL synchrotron. Since in the ARPES study the electron momentum determines the escaping angle of the photoelectrons with respect to the surface normal, electrons coming from inclined surface areas are detected under a different angle on the channel plate as illustrated in Fig. 4 (a) by a sketch of a structured sample with the resulting escaping angles for π-bands emerging from graphene on different parts of the sample. The inset in Fig. 4 (a) demonstrates, that for a scan along the $\overline{\Gamma K}$-direction of the graphene Brillouin zone of the flat surface area, the $\overline{K}$'-point of the faceted region would be recorded closer to the $\overline{\Gamma}$-point of the Brillouin zone of the flat graphene. Indeed, the exact position of the facet band depends both on the faceting angle and the photon energy. Fig. 4 (b) exhibits an ARPES-
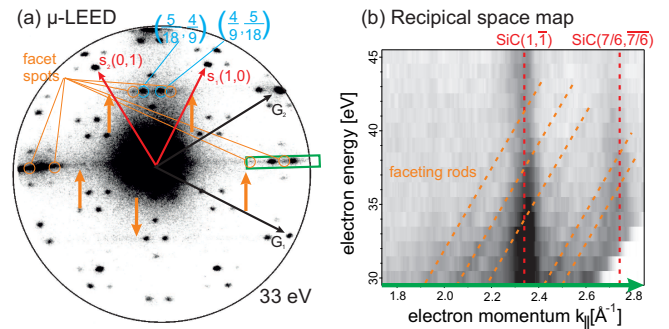
Figure 3 μ-LEED study of the structured and graphitized SiC-sample. (a) μ-LEED pattern taken on the structured part of the sample. The first order graphene and SiC diffraction spots are highlighted with black and red arrows, respectively. In addition, the typical superstructure spots of the $(6\sqrt{3}\times6\sqrt{3})$R30° reconstruction (some marked with blue circles) as well as faceting streaks (orange arrows) and faceting spots (orange circles) are visible. (b) Line profiles taken of the area indicated by the green rectangle in (a) for a series of electron beam energies (30-45 eV). The diffraction rods of the non-structured graphene areas are perpendicular (red dotted line), as expected in μ-LEED. In addition, several diffraction rods from the facets are visible and marked with orange dotted lines. They are inclined towards the rods from the non-structured surface areas.

scan on the structured and graphitized surface along the $\overline{\Gamma K}$-direction of the basal-plane graphene acquired using a photon energy of 100 eV. The main cone of the non-structured graphene which in this contrast setting is strongly overexposed is fitted by tight-binding simulations in a 2nd nearest neighbor model (red dotted line). Only one branch of the two graphene π-bands forming the Dirac cone is clearly visible when acquired along the $\overline{\Gamma K}$-direction due to destructive interference of the photoelectrons emitted from the two atoms per graphene unit cell [19, 20]. Next to the main cone a replica band can be located (green dotted line) which originates from the periodic reconstruction of the graphene/substrate interface. The replica is also observed on non-structured graphene samples [21]. However, the important band in this measurement is indicated by blue dotted line. It represents the linear π-band (Dirac cone) from the facet ribbon. Notably, the band velocity of the main cone and the replica band are similar indicating a similar graphene quality. Only the direction of the visible band branch is pointing to the opposite direction with respect to the one from the main cone, corroborating that this cone corresponds to the $\overline{K}$'-point of the ribbon. The faceting angle

(a)

(b)
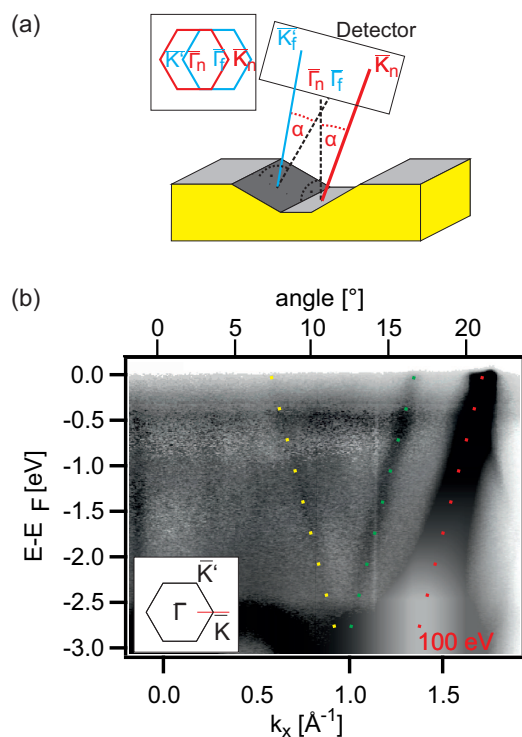
Figure 4 Expected and experimentally obtained electronic band structure of the structured graphene sample. (a) Schematic illustration of the influence of the inclination angle of the facets on the detection angle with respect to the expected signal position of the non-structured sample areas. In the inset the Brillouin zones of the facets and the flat graphene are mapped as they would appear with a changing angle between detector and sample. (b) Band structure E(k) slice acquired along the $\overline{\Gamma K}$-direction of the flat graphene using 100 eV photon energy. The dotted lines are tight binding model fits to the experimental band structure.

can be determined from the ARPES scan by the shift in angular position on the detector of the π-band emerging from the facets with respect to the one from the main cone. Here, a faceting angle of about 28° was determined from the experimental data (See supporting information for the angle determination). This result fits well with the angles obtained by AFM. Notably, we detect only one facet angle in ARPES in contrast to previous work [16, 22]. This could be due to the different SiC polytype used in our study (6H vs. 4H in the references) with different bilayer stacking sequence and - in consequence - different atomic surface structure of the facet(s). Yet, we should note that the secondary facets were reported [16, 22] as minority contribution (thus lower in intensity) and may just not be visible in our experiment.

Interestingly, in our study we did not observe the mini-bands, which were observed in other studies [22]. In contrast, we were able to detect the typical replica band beside the facet band, which demonstrates that the exact preparation steps and parameters are critical for the creation of well-ordered and homogeneous GNRs on SiC. Indeed, with the conventional, inhomogeneous growth in UHV, no graphene can be detected on the facets as shown in Fig. S2 of the supporting information.

4 Summary and Outlook

The growth of graphene on a SiC crystal structured into a periodic array of mesa and trench stripes was investigated by means of AFM, μ-LEED and ARPES. During the annealing steps the sidewalls of the trenches relax into facets. The faceting angle was determined to be about 26°-28° by AFM and ARPES measurements, which matches the results from previous studies. μ-LEED demonstrates that in the chosen direction of the stripe array, the graphene grown on the facet walls corresponds to armchair ribbons. A clear graphene band structure can be seen in ARPES on theses ribbons in contrast to earlier studies. Only one single band was observed, which implies a high degree of homogeneity of a graphene monolayer.

In this study the periodicity of the array and the depth of the trenches were chosen such that the ribbons have a suitable size (thus cover a sufficient portion of the surface) to monitor their properties by surface science techniques and determine precisely the optimum parameters to obtain monolayer graphene in the ribbon area. In a future step, the depth of the trenches can be reduced in order to generate small enough ribbons to reach the necessary confinement of the delocalized π-electron system to generate a band gap, which then can be analyzed by transport measurements, e.g. using a 4-point nanoprobe.

References

[1] K. Nakada, M. Fujita, G. Dresselhaus, and M. S. Dresselhaus, Phys. Rev. B **54**, 17954-17961 (1996).

[2] M. Y. Han, B. Özyilmaz, Y. Zhang, and P. Kim, Phys. Rev. Lett. **98**, 206805 (2007).

[3] F. Sols, F. Guinea, and A. H. C. Neto, Phys. Rev. Lett. **99**, 166803 (2007).

[4] J. Cai, P. Ruffieux, R. Jaafar, M. Bieri, T. Braun, S. Blankenburg, M. Muoth, A. P. Seitsonen, M. Saleh, X. Feng, K. Müllen, and R. Fasel, Nature **466**, 470 (2010).

[5] P. Ruffieux, J. Cai, N. C. Plumb, L. Patthey, D. Prezzi, A. Ferretti, E. Molinari, X. Feng, K. Müllen, C. A. Pignedoli, and R. Fasel, ACS Nano **6**, 6930 (2012).

[6] M. Sprinkle, M. Ruan, Y. Hu, J. Hankinson, M. Rubio-Roy, B. Zhang, X. Wu, C. Berger, and W. A. de Heer, Nat. Nanotech. **5**, 727 (2010).

[7] J. Baringhaus, M. Ruan, F. Edler, A. Tejeda, M. Sicot, A. Taleb-Ibrahimi, A.-P. Li, Z. Jiang, E. H. Conrad, C. Berger, C. Tegenkamp, and W. A. de Heer, Nature **506**, 349 (2014).

[8] M. S. Nevius, F. Wang, C. Mathieu, N. Barrett, A. Sala, T. O. Menteş, A. Locatelli, and E. H. Conrad, Nano Lett. **14**, 6080-6086 (2014).

[9] U. Starke and C. Riedl, J. Phys.: CM **21**, 134016 (2009).

[10] S. Forti, and U. Starke, J. Phys. D: Appl. Phys. **47**, 094013 (2014).

[11] S. Soubatch, S.E. Saddow, S.P. Rao, W.Y. Lee, M. Konuma, and U. Starke, Mat. Sci. Forum, **483-485**, 761-764 (2005).

[12] C. Riedl, U. Starke, J. Bernhardt, M. Franke and K. Heinz, Phys. Rev. B **76**, 245406 (2007).

[13] K. V. Emtsev, A. Bostwick, K. Horn, J. Jobst, G. L. Kellogg, L. Ley, J. L. McChesney, T. Ohta, S. A. Reshanov, J. Röhrl, E. Rotenberg, A. K. Schmidt, D. Waldmann, H. B. Weber, and T. Seyller, Nat. Mater. **8**, 203-207 (2009).

[14] X. Z. Yu, C. G. Hwang, C. M. Jozwiak, A. Köhl, A. K. Schmid, and A. Lanzara, J. Electron Spectr. Rel. Phen. **184**, 100-106 (2011).

[15] J. Baringhaus, J. Aprojanz, J. Wiegand, D. Laube, M. Halbauer, J. Hübner, M. Oestreich, and C. Tegenkamp, Appl. Phys. Lett. **106**, 043109 (2015).

[16] I. Palacio, A. Celis, M. N. Nair, A. Gloter, A. Zobelli, M. Sicot, D. Malterre, M. S. Nevius, W. A. de Heer, C. Berger, E. H. Conrad, A. Taleb-Ibrahimi, and A. Tejeda, Nano Letters **15**, 182 (2015).

[17] T. Filleter, K. V. Emtsev, T. Seyller, and R. Bennewitz, Appl. Phys. Lett. **93**, 133117 (2008).

[18] C. Klein, I. Heidmann, T. Nabbefeld, M. Speckmann, T. Schmidt, F.-J. Meyer zu Heringdorf, J. Falta, and M. Horn-von Hoegen, Surf. Sci. **618**, 109-114 (2013).

[19] E.L. Shirley, L.J. Terminello, A. Santoni and F.J. Himpsel, Phys. Rev. B **51**, 13614 (1995).

[20] I. Gierz, J. Henk, H. Höchst, C. R. Ast, and K. Kern, Phys. Rev. B **83**, 121408(R) (2011).

[21] A. Bostwick, T. Ohta, T. Seyller, K. Horn, and E. Rotenberg, Nat. Phys. **3**, 36-40 (2007).

[22] J. Hicks, A. Tejeda, A. Taleb-Ibrahimi, M. S. Nevius, F. Wang, K. Shepperd, J. Palmer, F. Bertran, P. Le Fèvre, J. Kunc, W. A. de Heer, C. Berger, and E. H. Conrad, Nat. Phys. **9**, 49-54 (2012).